RAA 2017 Vol. **17** No. **4**, 33 (12pp) doi: 10.1088/1674–4527/17/4/33

http://www.raa-journal.org *http://iopscience.iop.org/raa*

***R**esearch in*
***A**stronomy and*
***A**strophysics*

Numerical simulations of solar energetic particle event timescales associated with ICMEs

Shi-Yang Qi[1,2], Gang Qin[3,1,2] and Yang Wang[3]

[1] State Key Laboratory of Space Weather, National Space Science Center, Chinese Academy of Sciences, Beijing 100190, China

[2] College of Earth Sciences, University of Chinese Academy of Sciences, Beijing 100049, China

[3] School of Science, Harbin Institute of Technology, Shenzhen 518055, China; *qingang@hit.edu.cn*

Received 2016 July 19; accepted 2016 October 31

Abstract Recently, S. W. Kahler studied the timescales of solar energetic particle (SEP) events associated with coronal mass ejections (CMEs) from analysis of spacecraft data. They obtained different timescales for SEP events, such as *TO*, the onset time from CME launch to SEP onset, *TR*, the rise time from onset to half the peak intensity ($0.5I_{\rm p}$), and *TD*, the duration of the SEP intensity above $0.5I_{\rm p}$. In this work, we solve the transport equation for SEPs considering interplanetary coronal mass ejection (ICME) shocks as energetic particle sources. With our modeling assumptions, our simulations show similar results to Kahler's analysis of spacecraft data, that the weighted average of *TD* increases with both CME speed and width. Moreover, from our simulation results, we suggest *TD* is directly dependent on CME speed, but not dependent on CME width, which were not found in the analysis of observational data.

Key words: Sun: particle emission — Sun: flare — Sun: coronal mass ejections (CMEs)

1 INTRODUCTION

Solar energetic particle (SEP) events can mainly be divided into two classes through duration and intensity. The short-duration and low-intensity events, which are called impulsive events, are considered to be produced by solar flares. On the other hand, the longer duration and higher intensity ones, which are called gradual events, are considered to be produced by coronal and interplanetary shocks driven by coronal mass ejections (CMEs). It is interesting to study the relationship between properties of gradual SEP events and characteristics of the associated CMEs. With the first-order Fermi acceleration mechanism, Zank et al. (2000) introduced an onion shell model using a one-dimensional hydrodynamic code for the evolution of the CME-driven shock in the Parker model of interplanetary magnetic field (IMF). The model is only valid in strong shocks due to the Bohm diffusion coefficient used, so Rice et al. (2003) modified it to be usable with arbitrary strengths. In addition, Li et al. (2003) studied the transport of SEPs with their onion shell acceleration model considering the pitch angle scattering of particles without perpendicular diffusion. In their model, the pitch angle diffusion of charged particles is not considered between two consecutive pitch angle scatterings. Furthermore, Verkhoglyadova et al. (2009, 2010) adopted this model to study individual SEP events caused by CME shocks, and their simulation results can fit well with spacecraft observations for different elements. On the other hand, considering that interplanetary coronal mass ejection (ICME) shocks can continuously accelerate SEPs when propagating outward, Kallenrode & Wibberenz (1997); Kallenrode (2001) treated the ICME shock as a moving particle source. This model was adopted in a numerical code[1] by Wang et al. (2012) to study the transport of particles accelerated by an ICME driven shock in three dimensional solar wind and IMF including both parallel and perpendicular diffusion co-

[1] Hereafter, we denote the code as Shock Particle Transport Code, SPTC.

efficients. Furthermore, under varying perpendicular diffusion and shock acceleration strengths, Qin et al. (2013) reproduced the reservoir phenomenon with SPTC numerical simulations. In addition, with the same numerical modeling, Wang & Qin (2015) researched gradual SEP event spectra by focusing on spatial and temporal invariance. Finally, Qin & Wang (2015) compared the simulation results from SPTC with multi-spacecraft (*Helios 1*, *Helios 2* and *IMP 8*) observations during a gradual SEP event, and they obtained SPTC simulations which best fit the SEP event observed by spacecraft in different locations.

To investigate the relationship between properties of SEP events with the associated CMEs, Ding et al. (2014) studied the interaction of two CMEs that erupted nearby during a large SEP event by multiple spacecraft observations with the graduated cylindrical shell model. They obtained the solar particle release time and path length which indicated the necessary influence of the "twin-CME" (Li et al. 2012; Temmer et al. 2012) on the SEP event.

Because of the potentially large damaging effects caused by SEPs, the study of peak intensities of SEPs has become very important. Ding et al. (2015) presented new observational results of peak intensity with Fe/O ratio, which indicate the role of a seed population in extremely large SEPs. Reinard & Andrews (2006) studied the dependence of the occurrence and peak intensities of SEP events with properties of CMEs thoroughly using databases of LASCO/*SOHO* CMEs and *GOES* $E >$ 10 MeV protons. Besides peak intensities, timescales are another very important property of SEPs which could contribute to both space weather forecasting and understanding of the SEP injection profiles and propagation characteristics.

In order to study the properties and associations of SEP events, Cane et al. (2010) compared SEPs with flares and CMEs from 280 solar proton events which extended above 25 MeV. These occurred from 1997 to 2006 and were observed by near-Earth spacecraft. They divided the events into five groups according to the ratios e/p and Fe/O at event onset. Their results suggested that SEP event occurrence and peak intensities are more likely to be associated with faster and wider CMEs, especially with western CME source regions. Furthermore, Pan et al. (2011) investigated SEP timescales, such as the SEP onset time, the SEP rise time and the SEP duration. With an ice-cream cone model, Pan et al. (2011) studied LASCO/*SOHO* observation data of 95 CMEs associated with SEP events during 1998–2002, and came to the conclusion that the SEP onset time neither has a significant correlation with CME speed nor with CME width. They also suggested that the SEP rise time and the SEP duration have significantly positive correlations with radial speed and angular width of the associated CMEs, unless the events are not magnetically well connected to Earth.

Kahler (2013) researched the relationship between the EPACT/*Wind* 20 MeV SEP events timescales and their associated CME speed and widths observed by LASCO/*SOHO*. In Kahler (2013), 217 SEP events observed in a solar cycle during the period 1996–2008 were used. They defined the three characteristic times of the SEP events. The time from inferred CME launch at $1\,R_\odot$ to the time of the 20 MeV SEP onset at *Wind* was denoted as *TO*. The time from SEP onset to the time the intensity reached half of the peak value ($0.5I_{\rm p}$) was called *TR*; the time during which the intensity was above $0.5I_{\rm p}$ was named *TD*. From their results, they found that CME speed and width had a significant correlation and it is not easy to interpret the contribution of CME speed and width to timescales separately. Therefore, they suggested that faster and wider CMEs which drive shocks and accelerate SEPs over longer times would thus produce longer SEP timescales *TR* and *TD*.

In this paper, with the data used in the analysis by Kahler (2013), we study CME timescales by numerical simulations with SPTC, and we compare our results with those of Kahler (2013). In Section 2, we present the model. In Section 3, we describe the data analysis. In Section 4, we show our results. In Section 5, we present the conclusions and discussion.

2 MODEL

We model the transport of SEPs by following previous research (e.g., Qin et al. 2006; Zhang et al. 2009). The three-dimensional focused transport equation is written as (Skilling 1971; Schlickeiser 2002; Qin et al. 2006; Zhang et al. 2009)

$$\begin{aligned}\frac{\partial f}{\partial t} &= \nabla\cdot\Big(\kappa_\perp\cdot\nabla f\Big)+\frac{\partial}{\partial\mu}\Big(D_{\mu\mu}\frac{\partial f}{\partial\mu}\Big)\\ &\quad-\Big(v\mu\hat{\boldsymbol{b}}+\boldsymbol{V}^{\rm sw}\Big)\cdot\nabla f\\ &\quad+p\Big[\frac{1-\mu^2}{2}\Big(\nabla\cdot\boldsymbol{V}^{\rm sw}-\hat{\boldsymbol{b}}\,\hat{\boldsymbol{b}}:\nabla\boldsymbol{V}^{\rm sw}\Big)\\ &\quad+\mu^2\hat{\boldsymbol{b}}\,\hat{\boldsymbol{b}}:\nabla\boldsymbol{V}^{\rm sw}\Big]\frac{\partial f}{\partial p}-\frac{1-\mu^2}{2}\Big[-\frac{v}{L}\\ &\quad+\mu\Big(\nabla\cdot\boldsymbol{V}^{\rm sw}-3\hat{\boldsymbol{b}}\,\hat{\boldsymbol{b}}:\nabla\boldsymbol{V}^{\rm sw}\Big)\Big]\frac{\partial f}{\partial\mu},\end{aligned}\tag{1}$$

where $f(\boldsymbol{x}, \mu, p, t)$ is the gyrophase-averaged distribution function, $\boldsymbol{x}$ is the position in a non-rotating heliographic coordinate system, μ is the particle pitch-angle cosine, p is the particle momentum, v is the particle speed, t is time, $\boldsymbol{\kappa}_\perp$ and $D_{\mu\mu}$ are the particle perpendicular and pitch-angle diffusion coefficients, respectively, $\boldsymbol{V}^{\rm sw} = V^{\rm sw}\hat{\boldsymbol{r}}$ is the solar wind velocity which is in the radial direction, and $L = \left(\hat{\boldsymbol{b}} \cdot \nabla \ln B_0\right)^{-1}$ is the magnetic focusing length determined by the magnitude of the background magnetic field B_0 and the unit vector along the local magnetic field $\hat{\boldsymbol{b}}$. In Equation (1), almost all important transport effects are included, i.e., perpendicular diffusion (1st term on the right hand side (RHS)), pitch angle diffusion (2nd term on RHS), particle streaming along field line and solar wind flowing in the IMF (third term on RHS), adiabatic cooling in the expanding solar wind (4th term on RHS) and magnetic focusing in the diverging IMF (5th term on RHS). Here, the drift effects are neglected for lower-energy SEP transport in the inner heliosphere. Also, the IMF is modeled with the Parker field.

By following Burger et al. (2008), diffusion coefficients are determined. We set the perpendicular diffusion coefficient from nonlinear guiding center theory (Matthaeus et al. 2003) approximated with the analytical form according to Shalchi et al. (2004, 2010),

$$\boldsymbol{\kappa}_\perp = v l_d^{2/3} \lambda_\parallel^{1/3} \left(\mathbf{I} - \hat{\mathbf{b}}\hat{\mathbf{b}}\right), \tag{2}$$

where l_d is a parameter to control the value of the perpendicular diffusion coefficient. For simplicity, $\boldsymbol{\kappa}_\perp$ is set to be independent of μ with the assumption that particle pitch-angle diffusion is much faster than perpendicular diffusion, but generally μ dependent perpendicular diffusion coefficient should be used (e.g., Qin & Shalchi 2014).

The parallel particle mean free path $\lambda_\parallel$ is written as (Jokipii 1966; Hasselmann & Wibberenz 1968; Earl 1974)

$$\lambda_\parallel = \frac{3v}{8} \int_{-1}^{+1} \frac{(1-\mu^2)^2}{D_{\mu\mu}} d\mu, \tag{3}$$

and parallel diffusion coefficient $\boldsymbol{\kappa}_\parallel$ can be written as $\boldsymbol{\kappa}_\parallel = v\lambda_\parallel/3$.

We follow Beeck & Wibberenz (1986) and Teufel & Schlickeiser (2003) to model the pitch angle diffusion coefficient

$$D_{\mu\mu}(\mu) = G v R_L^{s-2} \left\{ |\mu|^{s-1} + h \right\} \left(1-\mu^2\right), \tag{4}$$

where G is a parameter to control the value of $D_{\mu\mu}(\mu)$, v is the particle speed and $R_L = pc/(|q|\,B_0)$ is the particle's Larmor radius. Here, a larger value of $h = 0.01$ is chosen for the non-linear effect of pitch angle diffusion at $\mu = 0$ in the solar wind (Qin & Shalchi 2009; Qin & Shalchi 2014).

To model particle injection, the shock is treated as a moving SEP source with the boundary condition (Kallenrode & Wibberenz 1997)

$$f_b = a\delta(r - v_{\rm s}t)\left(\frac{r}{r_c}\right)^{\alpha} \exp\left[-\frac{|\phi(\theta,\varphi)|}{\phi_c(p)}\right] p^{-\gamma} H(\phi_{\rm s} - |\phi(\theta,\varphi)|)\,, \tag{5}$$

where α and ϕ_c are the shock acceleration strength parameters. We assume ϕ_c to be a constant, but α to be a function of shock speed, e.g., we set

$$\alpha = \begin{cases} -3.5 & \text{if } v_{\rm s} < v_1\,, \\ v_{\rm s}/v_0 - 5 & \text{if } v_1 \le v_{\rm s} \le v_2\,, \\ -2 & \text{if } v_{\rm s} > v_2\,, \end{cases} \tag{6}$$

where $v_0 = 500$ km s^{-1}, $v_1 = 750$ km s^{-1} and $v_2 = 1500$ km s^{-1}. $\phi(\theta,\varphi)$ is the angle between source center and any point of particle injection (θ,φ). γ is the spectral index of source particles. In the simulations, we inject energetic particle shells with small space intervals Δr. $H(x)$ is the Heaviside step function, with $\phi_{\rm s}$ being the half angular width of the shock. A more detailed description of the shock model of our simulations can be referred to in Wang et al. (2012).

The transport Equation (1) is solved by a time-backward Markov stochastic process method (Zhang 1999) in the simulations. A detailed description of the method can be referred to in Qin et al. (2006). As mentioned in Section 1, our numerical code for transport of energetic particles with the CME driven shock as a moving particle source is denoted as the Shock Particle Transport Code, i.e., SPTC.

3 DATA ANALYSIS

We investigate 20 MeV proton intensity-time profiles of SEP events from 1996 to 2008 in order to compare with their associated CMEs. In particular, the SEP data are from the EPACT (von Rosenvinge et al. 1995) experiment on the *Wind* spacecraft, and information on their related CMEs is observed by LASCO/*SOHO* (Brueckner et al. 1995). Among all the 217 SEPs during this period (Kahler 2013), we study 204 SEPs whose CME parameters are available. In addition, for each event, the

CME solar source is determined by flare location, and the speed ($v_{\rm CME}$) and width ($W_{\rm CME}$) of the CME are obtained from Kahler (2013).

3.1 Parameter Selection

For grouping and selecting data, we follow the method suggested by Kahler (2013) of dividing the 204 events into five longitude ranges with about 41 events each, and subdividing each longitude range into several groups sorted by $v_{\rm CME}$ and $W_{\rm CME}$ respectively. The median values of longitude, $v_{\rm CME}$ and $W_{\rm shock}$ in each group are used as the characteristic values.

From data analysis of spacecraft observations, it is not easy to identify SEP onset time accurately, which is usually covered by the background of intensity. Therefore, in this work, we only focus on variation of *TD* with $v_{\rm CME}$ and $W_{\rm CME}$. To compare with observation, we obtain data analysis results on variation of *TD* with $v_{\rm CME}$ and $W_{\rm CME}$ from Kahler (2013) as shown in Table 1. From Table 1 we can see that we study SEP events with source location longitude in three ranges, W33−W60, W62−W90 and W100−bWL, with median values W48, W77 and W112, respectively. Note that bWL indicates sources behind the west limb. In each range of longitude, *TD* is shown to vary with median values of $v_{\rm CME}$ and $W_{\rm CME}$ by subdividing the range into several groups sorted by $v_{\rm CME}$ and $W_{\rm CME}$ respectively.

In order to study SEP timescales associated with CMEs, we use the SPTC described in Section 2 to simulate the transport of SEPs assuming the CME shock to be a moving particle source and that the shock nose is in the flare direction relative to the solar center. In SPTC, the speed of shock, $v_{\rm s}$, and the width of shock, $W_{\rm s}$, are needed. However, in analysis of spacecraft data from Kahler (2013), the speed and width of the CME are used instead. To compare the simulation results with analysis of spacecraft data, we need a model for the relationship between $v_{\rm s}$ and $v_{\rm CME}$, and that for the relationship between $W_{\rm s}$ and $W_{\rm CME}$. Firstly, we assume the speed of the CME is the same as that of the shock, $v_{\rm s} = v_{\rm CME}$. Secondly, since the width of shock ($W_{\rm s}$) is larger than that of the CME ($W_{\rm CME}$), we set,

$$W_{\rm s} = \begin{cases} W_{\rm CME} + \Delta W & \text{if } W_{\rm CME} < 360^\circ - \Delta{\rm W} \\ 360^\circ & \text{otherwise.} \end{cases} \quad (7)$$

By testing several values of ΔW, we finally set $\Delta W = 90^\circ$. It can be noted that such a kind of model for $W_{\rm s}$ is only an approximation, and it could lead to a discrepancy between observation and simulation results. So, we need to use a better $W_{\rm s}$ model in the future. Generally, the event source is near the solar equator, so the characteristic latitude of source location is set as 10° north. Other important simulation parameters that are not varied are shown in Table 2.

In order to investigate the relationship between solar wind speed $v_{\rm SW}$ and CME speed $v_{\rm CME}$, we obtain observational data on $v_{\rm SW}$ from the *Wind* spacecraft for the 204 CME events to fit the relationship between $v_{\rm CME}$ and $v_{\rm SW}$. It is shown that $v_{\rm CME}$ and $v_{\rm SW}$ are positively correlated. As we assumed above that $v_{\rm s} = v_{\rm CME}$, the relationship between $v_{\rm CME}$ and $v_{\rm SW}$ would turn to that between $v_{\rm s}$ and $v_{\rm SW}$. Thus $v_{\rm SW}$ can be represented by $v_{\rm s}$ as

$$v_{\rm SW} = 1.77 \times 10^{-5} {v_{\rm s}}^2 + 425, \quad (8)$$

where $v_{\rm SW}$ and $v_{\rm s}$ are in the unit of km s^{-1}. We also divide the events into several groups sorted by $v_{\rm CME}$, and obtain median values of $v_{\rm CME}$ as the characteristic ones for each group. So, we obtain the counterpart values $v_{\rm s}$ and $v_{\rm SW}$ through the assumption above; we use the characteristic ones in the simulations shown in Table 3. Table 3 also displays the other input parameters in each simulation coming from the characteristic values of $v_{\rm CME}$, $W_{\rm CME}$ and source location longitude picked up from Kahler (2013) shown in Table 1.

3.2 Simulation Output

For each data point, 3 200 000 virtual particles are calculated in our simulations. In our simulations, we obtain the time profiles of SEPs with characteristic speed and width of CMEs, with which we can get the SEP timescale, *TD*. For example, in Figure 1, we show simulation results of 20 MeV proton flux during an SEP event. In the simulation of Figure 1, we set solar wind speed to 502.2 km s^{-1}, longitude to 48° west, CME speed to 1600 km s^{-1} and CME width to 180°; other parameters are shown in Table 2. In Figure 1, the dotted line indicates the peak intensity ($I_{\rm p}$) of the event, and the dash-dotted line represents the half peak intensity. $T_{\rm s}$ and $T_{\rm e}$ signify the earliest and latest time when the intensity is half peak, respectively. So, we can obtain $TD = T_{\rm e} - T_{\rm s}$ from the time profile of the intensity from results of the simulation.

From the results of the simulations we can also get the weighted averages as follows. For example, in each range of shock speed and longitude, we have three ranges of shock width, so we have three values of *TD* from sim-

Table 1 Data Analysis Results of Variation of *TD* with $v_{\rm CME}$ and $W_{\rm CME}$ from Kahler (2013)

Source Location Longitude	W33–W60		W62–W90		W100–bWL	
TD varying with $v_{\rm CME}$	$v_{\rm CME}$ (km s^{-1})	*TD* (h)	$v_{\rm CME}$ (km s^{-1})	*TD* (h)	$v_{\rm CME}$ (km s^{-1})	*TD* (h)
	450	6.3	650	6.5	620	13.2
	800	12.0	1150	9.8	900	14.0
	1175	8.8	1450	21.3	1325	12.5
	1600	14.5	2100	18.1	1750	17.0
TD Varying with $W_{\rm CME}$	$W_{\rm CME}$ (°)	*TD* (h)	$W_{\rm CME}$ (°)	*TD* (h)	$W_{\rm CME}$ (°)	*TD* (h)
	77	8.3	133	7.8	100	7.5
	208	11.3	171	15.0	178	13.3
	360	15.8	360	16.4	360	17.2

Table 2 Model Parameters Used in the Calculations

Parameter	Physical meaning	Value
E	Particle energy	20 MeV
$r_{\rm O}$	Observer solar distance	1 AU
Δr	Shock space interval between two fresh injections	0.001 AU
r_c	Radial normalization parameter	0.05 AU
γ	Spectral index of source particles	-3.5
ϕ_c	Shock strength parameter	15°
$\lambda_{\parallel}$	Particle mean free path	0.16 AU
$\kappa_{\perp}/\kappa_{\parallel}$	Ratio between perpendicular and parallel diffusion coefficient	6.1%
r_{b0}	Inner boundary	0.05 AU
r_{b1}	Outer boundary	50 AU

Notes: For 20 MeV protons in the ecliptic at 1 AU.

Table 3 Shock Speed and Width, and Solar Wind Speed Used in all Simulations

Source location								
N10W48			N10W77			N10W115		
$v_{\rm s}$ (km s^{-1})	$v_{\rm SW}$ (km s^{-1})	$W_{\rm s}$ (°)	$v_{\rm s}$ (km s^{-1})	$v_{\rm SW}$ (km s^{-1})	$W_{\rm s}$ (°)	$v_{\rm s}$ (km s^{-1})	$v_{\rm SW}$ (km s^{-1})	$W_{\rm s}$ (°)
450	433.5	167	650	433.5	223	620	433.5	190
450	433.5	298	650	433.5	261	620	433.5	268
450	433.5	360	650	433.5	360	620	433.5	360
800	455.4	167	1150	455.4	223	900	455.4	190
800	455.4	298	1150	455.4	261	900	455.4	268
800	455.4	360	1150	455.4	360	900	455.4	360
1175	444.1	167	1450	444.1	223	1325	444.1	190
1175	444.1	298	1450	444.1	261	1325	444.1	268
1175	444.1	360	1450	444.1	360	1325	444.1	360
1600	502.2	167	2100	502.2	223	1750	502.2	190
1600	502.2	298	2100	502.2	261	1750	502.2	268
1600	502.2	360	2100	502.2	360	1750	502.2	360

ulation results with the same shock speed and longitude but different shock width. For the three ranges of shock width we can get their percentage according to the number of events, with which the weighted value of *TD* is obtained from the individual values of *TD*.

Furthermore, we study the relationship between CME speed and CME width using the observational data in Kahler (2013). We subdivide each longitude range into several groups sorted by CME width. We get the average CME speed for each group. The results are shown in

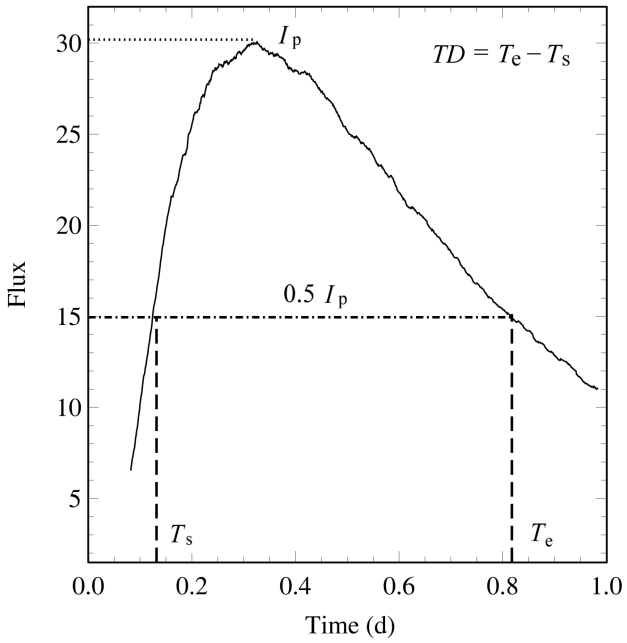

Fig. 1 Flux of 20 MeV proton during an SEP event with parameters shown in the text. The *dotted line* represents the peak intensity of the event, and the *dash-dotted line* signifies the half peak intensity. T_s and T_e indicate the earliest and latest time when the intensity is half peak, respectively.

Figure 2 as the relationship between the average of CME speed and the median value of CME width. The three data points in each longitude group of Figure 2 match those of the three CME width bins of Table 1. The line indicates fitting of the data. It is found that in terms of statistics, the average CME width increases with the increase of CME speed.

4 RESULTS

Figure 3 shows SEP timescale *TD* vs. CME speed for 20 MeV SEP events detected at 1 AU with different source locations in different panels. The the top, middle and bottom panels show different longitudes of source locations: 48° west, 77° west and 115° west, respectively. The black squares indicate spacecraft observation data in Table 1 which are obtained from the data analysis of Kahler (2013). The *TD* and CME speeds for each data point correspond to those in Table 1. The red triangles indicate the weighted average of simulations according to the distribution of number of events with different CME widths for any given CME speed interval obtained from the observational data in Kahler (2013) corresponding to the abscissa for black squares. The red and black dashed lines indicate the linear fitting of the weighted average simulation results represented by red triangles and that of spacecraft observation data represented by black squares, respectively. From Figure 3 we can see that the simulation results show a similar trend as the observation data, that is, the SEP timescale *TD* increases with CME speed.

Figure 4 shows a plot similar to Figure 3 except that the x-coordinate is CME width. The values for each of the black squares correspond to those of Table 1. The red triangles indicate the weighted average of simulation results according to the distribution of number of events with different CME speeds for any given CME width interval obtained from the observational data in Kahler (2013) corresponding to the abscissa for black squares. Similar to Figure 3, the red and black dashed lines indicate the linear fitting of the weighted average of simulation results and that of the spacecraft observation data, respectively. From Figure 4 we can see that, generally, the simulation results show a similar trend as observational data but with less slope, that is, the SEP timescale *TD* increases with CME width. However, from the top panel of Figure 4 (N10W48) the observational results show that the SEP timescale *TD* increases with CME width, but the simulation results show a constant for different CME widths. It can be noted that our simulations could deviate from observations due to modeling and statistical problems.

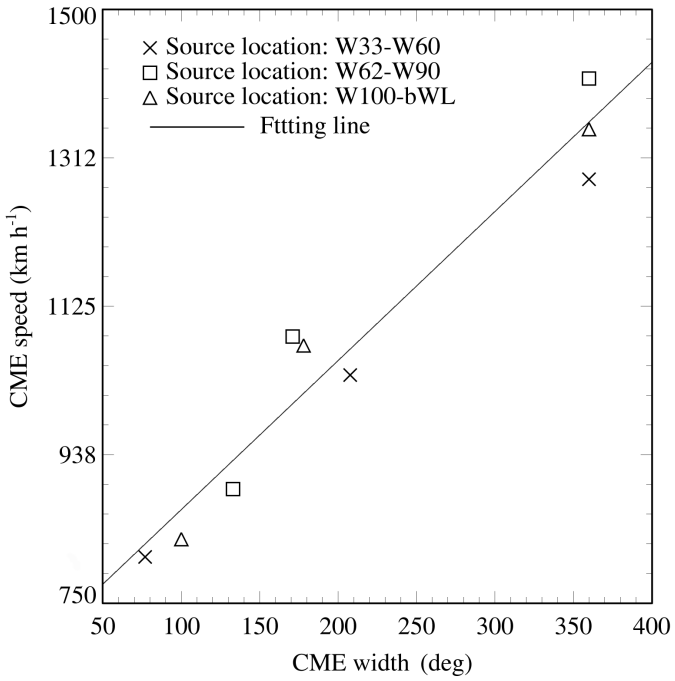

Fig. 2 Variations of CME speed as a function of CME width with different source location. *Crosses* represent average CME speed with CME width ranges in the source location range of W33–W60, *squares* are those of W62–W90, and *triangles* are those of W100–bWL. The *line* indicates fitting of the data. The symbols are from observation data analyzed by Kahler (2013).

For further study on the contribution of CME speed and width to timescales separately, we plot the individual simulations and weighted average of simulation results as follows.

Figure 5 shows simulations of SEP timescale *TD* vs. CME speed for 20 MeV SEP events detected at 1 AU with different source locations in different panels. Similar to Figure 3, the top, middle and bottom panels show different longitudes of source locations: 48° west, 77° west and 115° west, respectively. The yellow, green and blue triangles indicate simulations with different CME widths corresponding to those in Table 1. Each data point on a yellow line represents an individual simulation with a distinct CME speed but a common CME width of 133° and source location of N10W48, as do the green and blue lines with other source locations. Moreover, the values of all data points are shown in Table 3. The red triangles indicate the weighted average of simulations according to the distribution of the number of events with different CME widths for any given CME speed interval obtained from the observational data in Kahler (2013).

From simulation results shown in Figure 5, we can see that every single colored line increases, that is to say, for the same CME width, *TD* generally increases with increasing CME speed, and the weighted average of *TD* from simulations also generally increases with increasing CME speed. Another aspect is that the colored lines and symbols almost overlap. From triangles with a common abscissa but different colors we can see that when CME speed is fixed, values of *TD* with different CME widths are almost the same. In addition, when CME width is fixed, *TD* with different CME speeds increase. So, we suggest from our simulation that *TD* is dependent on CME speed but not on CME width, which the analysis of Kahler (2013) could not identify.

Figure 6 shows a plot similar to Figure 5 except that the x-coordinate is CME width. The yellow, green, light blue and purple triangles indicate simulations with different CME speeds corresponding to those of Table 1. Each data point on a yellow line signifies an individual simulation with a distinct CME width but a common CME speed of 450 km s^{-1} and source location of N10W48, as do the green and blue lines corresponding to other source locations. Moreover, the values of all data points are shown in Table 3. The red triangles indicate the weighted average of simulations according to the distribution of the number of events with different CME

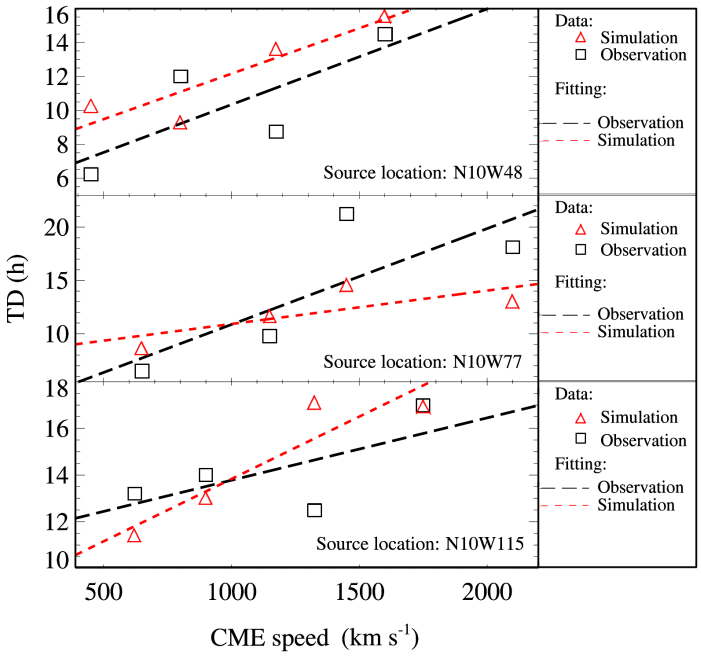

Fig. 3 SEP event timescale *TD* vs. CME speed. Different panels indicate different source locations. The *black squares* are from observational data analyzed by Kahler (2013). The *TD* and CME speed for each data point correspond to those of Table 1. The *red triangles* indicate weighted average of simulation results. The *black dashed lines* indicate linear fitting of observational data. The *red dashed lines* indicate linear fitting of the weighted average of simulation results.

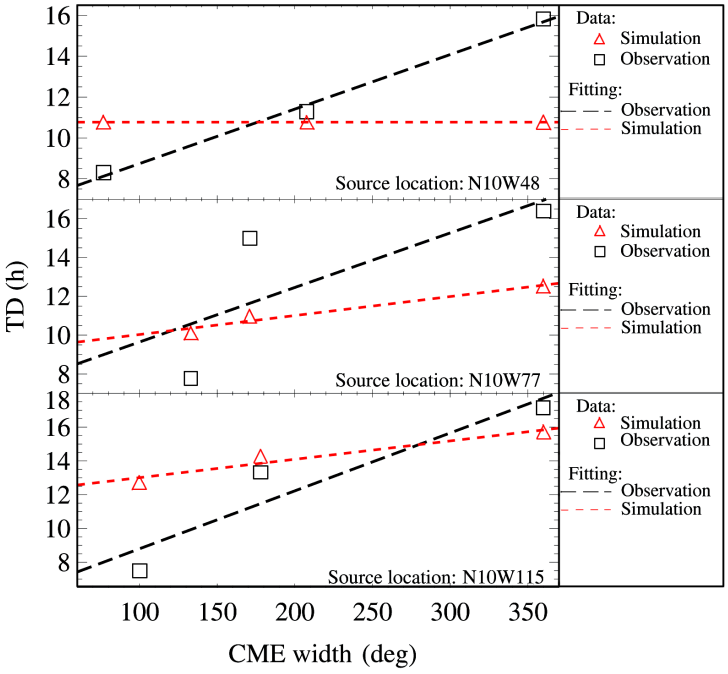

Fig. 4 SEP event timescale *TD* vs. CME width. Different panels indicate different source locations. The *black squares* are from observational data analyzed by Kahler (2013). The *TD* and CME widths for each of the data points correspond to those of Table 1. The *red triangles* indicate the weighted average from simulation results. The *black dashed lines* indicate linear fitting of observation data. The *red dashed lines* indicate linear fitting of the weighted average of simulation results.

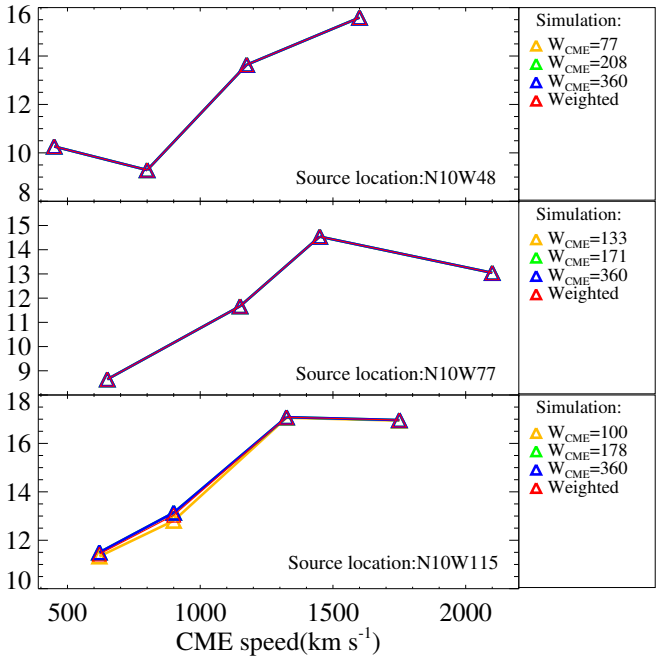

Fig. 5 Simulations of SEP event timescale *TD* vs. CME speed. Different panels indicate different source locations. The *yellow*, *green* and *blue triangles* indicate simulations with different CME widths. The *red triangles* indicate the weighted average of simulation results.

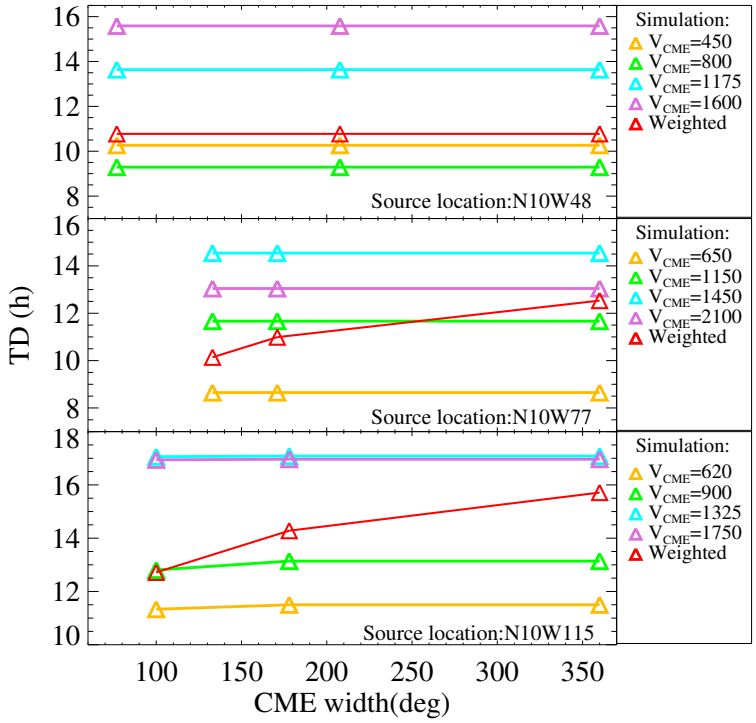

Fig. 6 Simulations of SEP event timescale *TD* vs. CME width. Different panels indicate different source locations. The *yellow*, *green*, *light blue* and *purple triangles* indicate simulations with different CME speeds. The *red triangles* indicate the weighted average of simulation results.

speeds for any given CME width interval obtained from the observational data in Kahler (2013).

From simulations used to construct Figure 6, we can see the yellow, green, light blue and purple lines are almost aclinic, that is to say, for the same CME speed, *TD* generally stays constant with different CME width. However, the red line which combines each individual line connecting data points from the same CME speed simulations with weighted average increases, that is to say, for the same CME width, *TD* increases with the increase of CME speed. In addition, the weighted average of *TD* increases with the increase of CME width. The reason is that with larger CME width it is more likely that CME speed becomes larger, so the weighted average of *TD* consequently becomes larger.

5 CONCLUSIONS AND DISCUSSION

Generally, accurate measurement of the first arriving particles in SEP events depends on the level of SEP flux background, so usually it is difficult to determine the timescales *TR*, *TO* and *TO+TR*. However, *TD*, which indicates the duration of the SEP intensity above $0.5I_{\rm p}$, has nothing to do with the first arriving particles, so the measurements of *TD* are relatively accurate. Therefore, we only study the timescale *TD*, but do not study *TR*, *TO* or *TO+TR*.

In this work, we use SPTC to simulate the transport of SEPs assuming the ICME shock is a moving particle source with parameters obtained from spacecraft observations analyzed by Kahler (2013), and other parameters set to typical values of SEP events. From simulations we get SEP timescale *TD* and compare with *TD* values from spacecraft data analysis by Kahler (2013). From spacecraft observations shown in Kahler (2013) we obtain the contribution of CME speed with the same CME width, and we also obtain that of CME width with the same CME speed. Finally, from simulation results of *TD* we can obtain the average of *TD* weighted with contributions from observations.

Our simulations show that with the same CME speed, *TD* stays constant with increasing CME width, but that the weighted average of *TD* increases with increasing CME width. Analysis of spacecraft data in Kahler (2013) demonstrates that *TD*, which is actually a weighted average, increases with the increase of CME width. In addition, our simulations indicate that with the same CME width, *TD* increases with the increase of CME speed, and that the average of *TD* increases with the increase of CME width. Analysis of spacecraft data in Kahler (2013) shows that the weighted average of *TD* increases with the increase of CME speed. Our simulations generally agree with analysis of spacecraft observational data from Kahler (2013) that the weighted average of *TD* increases with both CME speed and width. Furthermore, with our modeling assumptions, our simulations indicate some results not described in Kahler (2013) that *TD* is directly dependent on CME speed, but independent of CME width.

In order to study whether *TD* increases with CME width or speed by using observational data, one should choose SEP events with the same CME speed but different CME width to investigate if *TD* increases with CME width, and also one should choose SEP events with the same CME width but different CME speed to check if *TD* increases with CME speed. Kahler (2013) did not do this because of a limited number of events. However, simulations do not have this limitation, which offers us physical insights behind the observations. We compare the weighted average of simulations to the result of Kahler (2013), and we can demonstrate that the trend of our weighted average generally agrees with the result of Kahler (2013), so our work does not contradict the observational result of Kahler (2013). Moreover, our individual results can be used to show if *TD* depends on CME width with the same CME speed.

The model we use to calculate flux includes many effects, such as the source, parallel and perpendicular diffusion, adiabatic cooling, etc.; the overall effects can be very complicated, so we have to use numerical simulations to obtain results. It is possible in some cases that *TD* would decrease. But generally, *TD* has a trend to increase with the same CME width and increasing CME speed, and *TD* has a trend to be constant with the same CME speed and increasing CME width. Here, we compare the general trend between observations and simulations.

We choose shock model conditions to favor larger particle injections with increasing speeds and widths in order to compare with observations. There are some parameters arbitrarily chosen and fixed in all simulations; we tried different parameters, for example, we tested simulations with a different value of shock strength parameter ϕ_c, such as $10°$, $15°$, $18°$ and $25°$, and we found they would not change our general results. In the future, we plan to continue to study the effects of differing parameters in our model.

Observational evidences of the first detected SEP onsets or releases associated with good magnetic connection to source were discussed in Ding et al. (2016). In addition, Rouillard et al. (2011, 2012) suggested that SEP onsets could be considered associated with the modeled first connections of field lines to shocks. On the other hand, Qin & Wang (2015) showed the onsets from SPTC simulation results can fit well with those from observations of *Helios 1*, *Helios 2* and *IMP 8* at different longitudes simultaneously with perpendicular diffusion. It is interesting to compare the effects of these models carefully in the future.

There are many authors working on numerical simulations to produce SEP profiles from the shock onion shell model (e.g., Verkhoglyadova et al. 2009, 2010; Wang et al. 2012; Qin et al. 2013), and they usually study individual SEPs in detail; in this work, however, we are trying to study many SEPs with simulations so we can statistically compare with observations. CME width data from Kahler (2013) were observed by only one satellite, *SOHO*, so they lack determinacy. In the future, we plan to study CME data from multi-spacecraft observations. In addition, we would like to study the peak intensity of gradual SEP events associated with CMEs by comparing the simulations of SPTC with analysis of spacecraft data (e.g., Kahler & Vourlidas 2013).

Acknowledgements We are partly supported by the National Natural Science Foundation of China (Grant Nos. 41304135, 41574172, 41374177 and 41125016), the CMA (Grant GYHY201106011), and the Specialized Research Fund for State Key Laboratories of China. The computations were performed by Numerical Forecast Modeling R&D and the VR System of State Key Laboratory of Space Weather and Special HPC work station of the Chinese Meridian Project. CME data were taken from the CDAW LASCO catalog, which is generated and maintained at the CDAW Data Center by NASA and The Catholic University of America in cooperation with the Naval Research Laboratory. *SOHO* is a project of international cooperation between ESA and NASA. We thank D. Reames for the use of the EPACT proton data.

References

Beeck, J., & Wibberenz, G. 1986, ApJ, 311, 437
Brueckner, G. E., Howard, R. A., Koomen, M. J., et al. 1995, Sol. Phys., 162, 357
Burger, R. A., Krüger, T. P. J., Hitge, M., & Engelbrecht, N. E. 2008, ApJ, 674, 511
Cane, H. V., Richardson, I. G., & von Rosenvinge, T. T. 2010, Journal of Geophysical Research (Space Physics), 115, A08101
Ding, L.-G., Cao, X.-X., Wang, Z.-W., & Le, G.-M. 2016, RAA (Research in Astronomy and Astrophysics), 16, 005
Ding, L.-G., Li, G., Le, G.-M., Gu, B., & Cao, X.-X. 2015, ApJ, 812, 171
Ding, L.-G., Li, G., Jiang, Y., et al. 2014, ApJ, 793, L35
Earl, J. A. 1974, ApJ, 193, 231
Hasselmann, K., & Wibberenz, G. 1968, Z. Geophys., 34, 353
Jokipii, J. R. 1966, ApJ, 146, 480
Kahler, S. W. 2013, ApJ, 769, 110
Kahler, S. W., & Vourlidas, A. 2013, ApJ, 769, 143
Kallenrode, M.-B. 2001, J. Geophys. Res., 106, 24989
Kallenrode, M.-B., & Wibberenz, G. 1997, J. Geophys. Res., 102, 22311
Li, G., Moore, R., Mewaldt, R. A., Zhao, L., & Labrador, A. W. 2012, Space Sci. Rev., 171, 141
Li, G., Zank, G. P., & Rice, W. K. M. 2003, Journal of Geophysical Research (Space Physics), 108, 1082
Matthaeus, W. H., Qin, G., Bieber, J. W., & Zank, G. P. 2003, ApJ, 590, L53
Pan, Z. H., Wang, C. B., Wang, Y., & Xue, X. H. 2011, Sol. Phys., 270, 593
Qin, G., Zhang, M., & Dwyer, J. R. 2006, Journal of Geophysical Research (Space Physics), 111, A08101
Qin, G., & Shalchi, A. 2009, ApJ, 707, 61
Qin, G., Wang, Y., Zhang, M., & Dalla, S. 2013, ApJ, 766, 74
Qin, G., & Shalchi, A. 2014, Physics of Plasmas (1994-present), 21, 042906
Qin, G., & Shalchi, A. 2014, Applied Physics Research, 6, 1
Qin, G., & Wang, Y. 2015, ApJ, 809, 177
Reinard, A. A., & Andrews, M. A. 2006, Advances in Space Research, 38, 480
Rice, W. K. M., Zank, G. P., & Li, G. 2003, Journal of Geophysical Research (Space Physics), 108, 1369
Rouillard, A. P., Odstřcil, D., Sheeley, N. R., et al. 2011, ApJ, 735, 7
Rouillard, A. P., Sheeley, N. R., Tylka, A., et al. 2012, ApJ, 752, 44
Schlickeiser, R. 2002, Cosmic Ray Astrophysics (Berlin: Springer)
Shalchi, A., Bieber, J. W., Matthaeus, W. H., & Qin, G. 2004, ApJ, 616, 617
Shalchi, A., Li, G., & Zank, G. P. 2010, Ap&SS, 325, 99
Skilling, J. 1971, ApJ, 170, 265
Temmer, M., Vršnak, B., Rollett, T., et al. 2012, ApJ, 749, 57
Teufel, A., & Schlickeiser, R. 2003, A&A, 397, 15

Verkhoglyadova, O. P., Li, G., Zank, G. P., Hu, Q., & Mewaldt, R. A. 2009, ApJ, 693, 894
Verkhoglyadova, O. P., Li, G., Zank, G. P., et al. 2010, Journal of Geophysical Research (Space Physics), 115, A12103
von Rosenvinge, T. T., Barbier, L. M., Karsch, J., et al. 1995, Space Sci. Rev., 71, 155
Wang, Y., & Qin, G. 2015, ApJ, 806, 252
Wang, Y., Qin, G., & Zhang, M. 2012, ApJ, 752, 37
Zank, G. P., Rice, W. K. M., & Wu, C. C. 2000, J. Geophys. Res., 105, 25079
Zhang, M. 1999, ApJ, 513, 409
Zhang, M., Qin, G., & Rassoul, H. 2009, ApJ, 692, 109